Numerical modeling of flow control on a symmetric aerofoil via a porous, compliant coating

Divya Venkataraman[a)] and Alessandro Bottaro
DICAT - Department of Civil, Environmental and Architectural Engineering,
University of Genoa, Italy

A passive actuation technique, that entails covering the suction side of an aerofoil with a poro-elastic carpet, is presented. Numerical modeling of the coupled fluid-structure interaction problem is performed for a low Reynolds number regime, characteristic of micro aerial vehicles. The immersed boundary technique is employed, which offers the advantage of using Cartesian grids for complex geometries. By suitably selecting the characteristics of the carpet, to synchronise characteristic time scales of the fluid and the structural systems, significant drag reduction and/or lift enhancement can be achieved, associated with modifications of the length scales of the shed vortices and a mild intensification of their intensity. A parametric analysis shows that such a coating is able to affect the topology of the flow in the proximity of the rear of the aerofoil, by adapting spontaneously to the separated flow. © *2012 American Institute of Physics*. [http://dx.doi.org/10.1063/1.4748962]

I. INTRODUCTION

Optimization of flight performance, by manipulating fluid flows and controlling boundary-layer separation, has been a very active research area for a number of years now – be it in terms of increasing the mean lift, delaying stall, noise reduction, and optimization of fuel use achieved by decreasing the drag or even influencing the transition to turbulence.[1] Apart from the immediate implications of flight optimization in the commercial arena, these goals are also sought while designing unmanned aerial vehicles (UAVs) and micro aerial vehicles (MAVs). These devices, which usually operate at low Reynolds numbers, have many issues associated with their design – such as size limitations, high efficiency, high manoeuvrability, and noise reduction – each of which has immediate applications to various problems that they can tackle.[2] For instance, high manoeuvrability, like in insect flight, is desirable in applications such as earthquake search-and-rescue operations or exploring a radioactivity-contaminated building. Issues such as trade-off between size limitations and high efficiency become pertinent in the design of light MAVs with acceptable lifetimes powered by batteries. Finally, noise reduction is important in military operations, to ward off the threat of being detected by enemy detection systems. Considering the amount of innovation that goes behind all this, it is particularly worthwhile to analyse and emulate efficient flying mechanisms observed in nature, in the form of birds and insects. These mechanisms smartly optimize unsteady aerodynamics to their advantage,[3,4] having evolved and adapted over millions of years, and having stood the test of time.

One such noteworthy instance is that of covert feathers over the wings of some birds, which "pop-up" automatically from the wings when the birds experience a drop in their flying abilities. This happens particularly during landing or gliding phases, when a high angle of attack is needed to produce sufficient aerodynamic lift (cf. Figure 1). As an example, for perching manoeuvre during landing, there is evidence of coverts popping up and vibrating when birds employ high angles of attack. These feathers, or passive actuators, adapt their movement to the local, instantaneous

---

[a)]Author to whom correspondence should be addressed. Electronic mail: divya@dicat.unige.it.

24, 093601-1   © 2012 American Institute of Physics

FIG. 1. Snapshot of an egret that is landing. Small covert feathers can be seen prominently popping up towards the root of each wing. (Photo courtesy of J R Compton - Copyright 2008.)

flow and control many undesirable physical phenomena that lead to a decrease in the aerodynamic performance. This has interesting applications for MAVs that operate at high angles of attack, though the Reynolds number regimes are much lower.

An interesting aspect of flight observed in nature is that it spans a wide range of chord-Reynolds numbers, starting from as low as about 1000 for insects such as houseflies or mosquitoes, to around 100 000 or more for birds such as eagles. The key to effectively implementing the envisaged passive controls on aerodynamic configurations, thus highly depends on the understanding of the physics occurring across this wide spectrum of Reynolds numbers. For example, in the low Reynolds number regime, of the order of 1000, viscous forces are significant. As a consequence, there is increased drag and reduced lift-to-drag ratio; moreover, flows with low Reynolds numbers usually maintain laminarity, whereas higher Reynolds number flows are often subject to transition to turbulence, whose prevention is itself a fluid-dynamic challenge in its own right.[5,6] Many natural flyers, on account of flying at relatively low Reynolds numbers, restrict themselves to maintaining laminar flow, which, in general, is less capable of handling adverse pressure gradients in the boundary layer and thus is more susceptible to separation, when compared to a turbulent boundary layer. To study the effect of covert feathers in a relatively simple setup that is also closer to flight observed in nature, separation control for a laminar flow is chosen as the scope of this paper.

The management of flow separation in this regime becomes crucial for designing MAVs and UAVs. In fact, aerodynamic and propulsion factors put severe constraints on MAVs, like narrow ranges of airspeed as well as angle of attack, rendering the vehicle more vulnerable to gust upset. Shape optimization (or morphing) techniques with the use of passive actuators or flaps, indeed seem to have the ability to generate aerodynamic forces and moments required to stabilize and manoeuvre MAVs, without penalizing their weight and energy constraints. In the recent past, the research and design of fixed-wing MAVs has focussed on low Reynolds number regimes, where a fixed wing has inferior performance compared to MAVs with flapping or rotary wings.

The study of flow past a layer of feather-like protrusions or in the presence of some roughness on aerodynamic surfaces is useful even outside the realm of aerospace and related applications. For instance, in the study of thick bundles of immersed vegetation and wind-exposed plants, the plant movement coupled with the nearby fluid flow leads to a frequency lock-in mechanism and vortex induced vibrations, which are known to affect the plant growth.[7,8] Similarly, in the design of sports balls, it is desirable to have some roughness on the surface, so that the balls yield optimum performance and are subject to acceptable wear-and-tear.[9]

Despite the difficulty of modern observation methods to keep an instant-by-instant account of the details of the fast motion of birds, the covert feathers are believed to control flow separation, by storing and then releasing energy in the boundary layer, according to the instantaneous fluid flow. This, in turn, is thought to affect the vortex shedding by trapping a vortex in front of the feathers, thus filling in the angle between the aerofoil and the feathers, and so, restricting the shed

vortices to the hind part of the aerofoil.[10] Hence, there is a resultant delay in stall and a possible explanation to the efficient flight of birds under conditions of high angles of attack or in gusty winds. These feathers act as sensors to reverse flow (which is consequently followed by separation) and are activated automatically at the appropriate time. Thus, this feature of automatic activation, as opposed to active control techniques which require an energy input to come into action, provides industry with yet another reason to study ways to mimic this mechanism. Much experimental[11–15] as well as computational work[16–18] has been done simulating this behaviour and the results obtained indeed prove the effectiveness of a poro-elastic coating over a surface. For instance, a substantial drop in the mean drag, lift, and drag fluctuations, as well as a noteworthy increase in mean lift, has been observed.[16,17]

In this paper, a homogenized model of feather coating is considered, as described in later sections. The coating has the following key features which emulate the important properties of birds' feathers:

(1)   Porosity: the fluid can flow through the layer of feathers.
(2)   Anisotropy: the fluid is oriented along a specific direction as it enters the layer.
(3)   Compliance: the layer can deform and adapt to the surrounding flow.

It should be noted that the design considerations of such passive actuators should also take into account the basic premise that these control elements, when not in use (or in situations of low or moderate angles of attack), should not have any negative impact on the quality of the flow past the aerofoil.

Here, the shape adaptation abilities of this porous, compliant coating is tested numerically in two dimensions and interpreted for separated flow on a symmetric aerofoil at a chord-based Reynolds number Re equal to 1100. The numerical setup and the modeling assumptions are presented to highlight the dynamics of the fluid and structure parts, as well as the coupling between the two. This paper aims to extend the study of the effectiveness of a feather coating on a circular cylinder,[17] to a stream-lined body of an aerofoil. It is to be noted that in this case it becomes more important to resolve the flow structures close to the body, owing to the increased complexity of the shape.

Schematically, the computational domain is divided into three parts: the solid body or the aerofoil, the surrounding fluid in movement, and a mixed fluid-solid part corresponding to the poro-elastic, compliant coating. The assumptions on state variables are that there is no mass exchange between the fluid and solid parts; and the temperature is constant at all times.

Section II outlines the numerical method briefly (the details of which can be found in Ref. 17), and also validates the computational code showing some convergence tests. Section III presents some results showing increase in aerodynamic efficiency, and outlines the methods adopted to arrive at a control-effective set of physical and structural parameters for the coating. Sections IV and V of this paper, respectively, interpret the physics behind the performance enhancement and give conclusions, perspectives, and generalizations to this work.

II. PHYSICAL MODEL AND COMPUTATIONAL METHOD

A. Fluid domain equations and their numerical resolution

The simulation of the unsteady flow around the NACA0012 aerofoil, which is symmetric about its mean camber line, is done by directly resolving the incompressible Navier-Stokes and continuity equations on a Cartesian grid in a two-dimensional periodic domain by means of the immersed boundary method.[19] These equations in normalized form are given by

$$\frac{\partial \vec{U}}{\partial t} + (\vec{U} \cdot \nabla)\vec{U} = -\nabla p + \frac{1}{Re}\nabla^2 \vec{U} + \vec{F}; \nabla \cdot \vec{U} = 0, \qquad (2.1)$$

where $\vec{U}$ is the Eulerian velocity, p is the pressure, Re is the Reynolds number based on the free-stream velocity and the aerofoil chord length D, and $\vec{F}$ is a volume force accounting for the effects of boundaries immersed in the domain, namely, the aerofoil, the coating layer, and a buffer zone. The buffer zone, located towards the end of the computational domain, plays the role of damping

the unsteady structures in the aerofoil's wake, before they reach the end of the domain. Besides, it also enforces the periodic inflow-outflow condition on the velocity field.

The total force $\overrightarrow{F}$ is thus decomposed into three components, namely $\overrightarrow{F}^{a}$, $\overrightarrow{F}^{b}$, and $\overrightarrow{F}^{c}$ (for the aerofoil, buffer zone and coating layer, respectively), where the first two components have a general form given by

$$\overrightarrow{F} = M\left\{ \alpha \int_0^t (\overrightarrow{U^{des}} - \overrightarrow{U})dt + \beta(\overrightarrow{U^{des}} - \overrightarrow{U}) \right\}. \tag{2.2}$$

That is, $\overrightarrow{F}^{a}$ and $\overrightarrow{F}^{b}$ are the (non-dimensional) forces that, like damped harmonic oscillators, bring the fluid velocities on the boundaries back to the values desired on them (denoted by U^{des}, and which are $\overrightarrow{0}$ for the aerofoil and the free-stream velocity $\overrightarrow{U_\infty} = (u_\infty, 0)$ for the buffer layer), whenever they start differing. It can be seen that the first term on the right hand side of Eq. (2.2) is a restoring force-type term, while the second term is the resistance offered by the boundary to assume the value $\overrightarrow{U^{des}}$ different from $\overrightarrow{U}$. This formulation of the immersed boundary method is referred to as *feedback forcing*.[20] The term M denotes a smooth scalar function corresponding to dimensionless density, and for both the aerofoil and the buffer zone, has forms like hyperbolic functions and assumes a value equal to one inside the immersed boundaries, and zero outside them. The parameters α and β, which are positive constants corresponding to dimensionless acceleration per unit mass and velocity per unit mass, respectively, are chosen suitably so that the difference between the desired and the actual velocities, within and on the immersed boundary, is below a sufficiently small threshold value, and hence zero for practical purposes. Further, an appropriate selection of these parameters for the buffer zone ensures that no dominant frequencies in the flow enter the inlet due to the periodic boundary condition.

$\overrightarrow{F}^{c}$ is the force due to the compliant coating, to obtain which again multiplication by a scalar field M^c (similar to M above) is involved. Some of these details will be outlined in Section II C 1.

Equations (2.1) are solved by employing a three-step projection approach on a staggered grid, in which the convective terms are treated using explicit Adams-Bashforth, the viscous terms by semi-implicit Crank-Nicolson and the pressure correction equation by conjugate gradient methods. All the variables are periodic in the spatial directions. The aerodynamic performance is measured in terms of the non-dimensional time-averaged drag and lift coefficients, obtained by integrating the horizontal and vertical components of the total force over the aerofoil. More details on the numerical technique and suitable immersed boundary force parameters can be found in Ref. 17.

B. Numerical convergence of the fluid model

Since a Cartesian grid is used for the computations, which is non-conformal to the shape of the aerofoil, the mesh is concentrated near the aerofoil, to resolve the wake near it, and sparse far away from it (cf. Figure 2).

At $Re = 1100$, given a fixed grid size, it is seen that whereas for a relatively small angle of attack, a domain with dimensions $60D \times 30D$ gives grid-converged results, for angles of attack of around
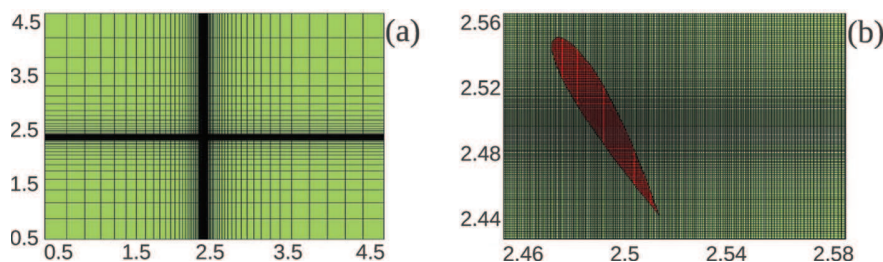

FIG. 2. (a) Distribution of grid points over the whole computational domain; only one in every 10 lines is shown; the aerofoil is at the domain's centre, at the intersection of the horizontal and vertical black bands. (b) Detail of the grid in the vicinity of the aerofoil.
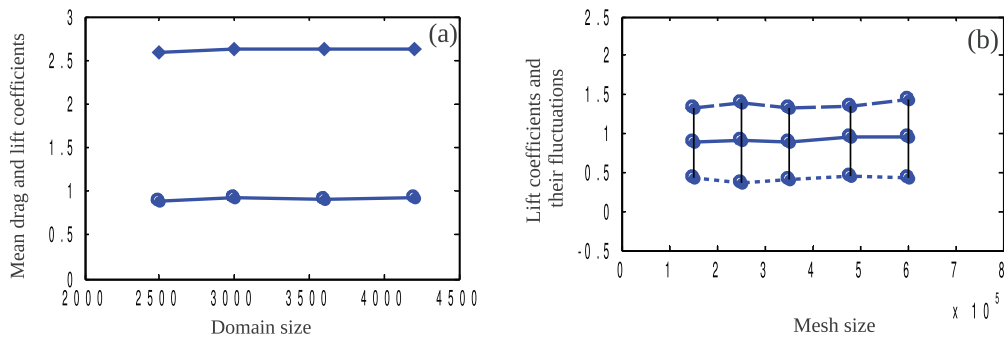
FIG. 3. Spatial convergence of fluid solver. (a) Mean lift (bottom) and mean drag (top) coefficients as functions of domain size (in units of D^2), with mesh size fixed to 700×500. (b) Mean lift coefficient, together with the instantaneous maximum and minimum values during an oscillation cycle, as functions of the total number of grid points for a domain size fixed to $50D \times 50D$.

$40°$ going to high angles of around $70°$, a domain with transverse length of $50D$ or more (possibly, as big as $80D$) is required. Once an optimal domain is decided upon, grids with a number of cells ranging from 500×300 to 1000×600 cells are tested to decide on the optimal grid. For instance, at $70°$, the domain $50D \times 50D$ with 700×500 cells has been found to provide grid-converged average lift and drag coefficients (cf. Figure 3).

C. Feather layer model

Since the porous, compliant coating is meant to mimic a dense cluster of feathers (which is unfeasible to model owing to very large number of degrees of freedom), a discrete number of reference beams, homogeneously spread over the layer, is chosen to approximate the anisotropic compliant coating of variable porosity (cf. Sec. I). Each reference beam is a rigid circular cylinder, surrounded symmetrically by a control volume (cf. Figure 4(a)). The dynamics of the reference beams, which are modelled as being connected to each other by nonlinear dampers and springs, is solved by a set of nonlinear dynamical equilibrium equations (which will be indicated in Sec. II C 2). The coupling between the fluid and structure is outlined next.

1. Coupling between fluid and structure

The interaction between the fluid and the coating is estimated as the drag force past a cluster of long thin cylinders. This force per unit volume $\overrightarrow{F}^c$ is split into the two components tangential and normal to each such thin cylinder, of magnitudes F_t^c and F_n^c, respectively. To approximate these,
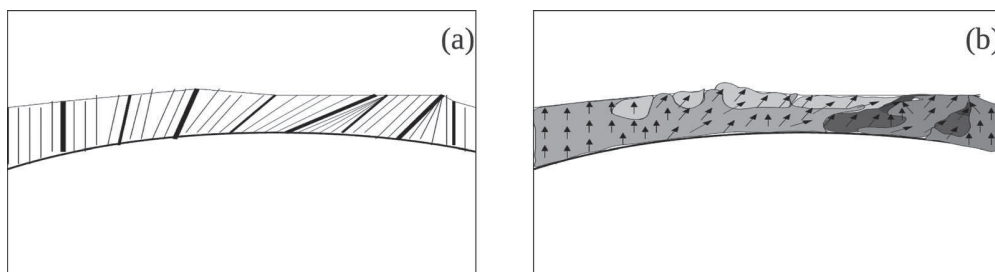

FIG. 4. Feather layer model. (a) Homogenized approach; the thickest lines are the reference beams, each of them being surrounded by control volumes. The position and velocity of individual elements in a control volume (shown by thin lines) is interpolated from the position and velocity of the reference beams. (b) Representation of the variable porosity (in terms of the packing density variable) and anisotropy (in terms of the orientation vector) of the layer – a darker shade stands for higher packing density.

two variables are defined, namely the packing density ϕ, which captures the variable porosity of the coating, and the unit orientation vector $\vec{d}$ of each feather in the control volumes, which measures the anisotropic nature of the layer (cf. Figure 4(b)). The packing density is defined by $\phi = \frac{V_{feather}}{V_{layer}}$, or the ratio of the volume occupied by the feathers over the total sampling volume. Hence, it varies continuously with time between 0 and 1 within the coating.

The mathematical formulation for the magnitudes of these tangential and normal force components is derived under the assumptions that, there is steady axisymmetric flow in the Stokes' regime between concentric cylinders, and that the local Reynolds number (based on the velocity of the fluid in the porous layer and the diameter of a reference beam) is of moderate value (i.e, having a magnitude of less than or equal to order 2), respectively. The details of these formulae as well as their derivation are indicated in Ref. 17. These force components, which are obtained for each grid point in the control volumes are transferred to the frame of the reference beams, by integration over each control volume.

It should be noted that the normal and tangential components of the force are respectively dependent on the normal and tangential velocity components,[17] which in turn are dependent on the angles made by each of the reference beams with the aerofoil surface, and vice-versa. As a consequence, depending on whether the normal or tangential force contributions is greater, the feathers have a tendency to either favour or oppose alignment with the free-stream flow. In this model, the condition is imposed on the reference beams that they should never make a $90°$ or an obtuse angle to the free-stream flow.

2. Dynamics of the compliant coating

The forces in action are taken to be concentrated on N reference beams. The motion of such thin rigid circular-cylindrical beams, hinged to the aerofoil surface, of length l and diameter d_c, are found in terms of the angular displacement about their equilibrium angle θ_{eq}, denoted by $\theta(1), \dots, \theta(N)$. All angles involved in the structure model are defined with respect to the positive horizontal axis. The different moments that are considered in the model are now illustrated (cf. Figure 5).

Rigidity: Each reference beam can oscillate within a sector$[\theta_{min}, \theta_{max}]$ around its equilibrium angle θ_{eq}, its angular frequency being controlled by the rigidity parameter K_r (having dimensions $[M][L]^2[T]^{-2}$). The rigidity moment is then given by

$$M_{rigidity}(k) = -K_r f_1[\theta(k)], \tag{2.3}$$

where $f_1[\theta(k)]$ is a nonlinear function dependent on the parameters θ_{eq}, θ_{max}, and θ_{min} (cf. Ref. 17). Further, f_1 is always an increasing function of θ which vanishes at θ_{eq}, hence forcing the magnitude of the rigidity moment to be greater when it is farther away from θ_{eq} and close to zero in the neighbourhood of θ_{eq} (displaying a linear trend with θ), exactly like the restoring force in a spring-mass system.

Interaction: Each reference beam is linked to its adjacent beams by nonlinear springs of stiffness K_i (having same dimensions as K_r), with progressive increase in the interaction moment as two adjacent beams approach one another. This feature is modelled in the expression for the interaction
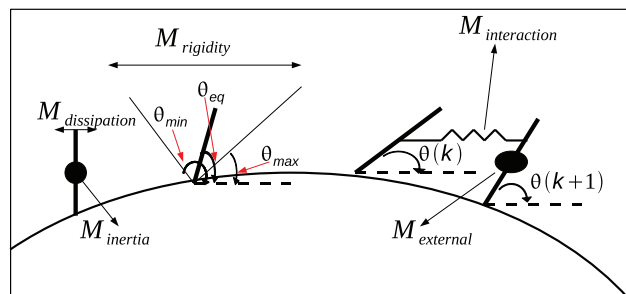

FIG. 5. Moments in the structure model.

moment (which is qualitatively similar to the expression for the rigidity moment) by means of the nonlinear function $f_2[\theta(k)]$, dependent on $\theta(k+1)$, h (the distance between two adjacent beams) and l (the beam's length) (cf. Ref. [17]).

Dissipation: This takes into account the energy dissipation due to plastic deformation of each beam and friction between adjacent feathers, and is given by

$$M_{dissipation}(k) = -K_d\dot{\theta}(k), \tag{2.4}$$

where K_d is the dissipation parameter (having dimensions $[M][L]^2[T]^{-1}$) that controls the magnitude of the energy lost.

Inertia: This moment is by virtue of the total mass M of all the feathers present in the control volume surrounding a reference beam, and is given by

$$M_{inertia}(k) = M(\frac{l}{2})^2\ddot{\theta}(k). \tag{2.5}$$

External force from fluid: This force is obtained by integrating the volume force F^c over the control volume surrounding each reference beam, $V_{control}(k)$. It is given by

$$M_{external} = \frac{l}{2}F_{ext}(k) = \frac{l}{2}\int_{V_{control}(k)}\|F_n^c\|dV, \tag{2.6}$$

because the tangential component F_t^c of the external force exerts no moment.

3. Non-dimensional model for the compliant coating

The dynamic equilibrium of the system of all reference beams is found by balancing the above moments for each element. To compare the frequencies present in the structure with those in the flow, characteristic frequencies corresponding to the rigidity, interaction, and dissipation moments are defined by $\omega_r = \sqrt{K_r/Ml_c^2}$, $\omega_i = \sqrt{K_i/Ml_c^2}$, and $\omega_d = K_d/Ml_c^2$, respectively.[7] To limit the number of independent parameters, the structure model is taken to be dominated by rigidity effects. The equation in dimensionless form is given by

$$\ddot{\theta} + \gamma\dot{\theta} + f_1(\theta) + \kappa f_2(\theta) = \mu_{ext}. \tag{2.7}$$

Here the parameters γ and κ are defined as ω_d/ω_r and ω_i^2/ω_r^2, respectively, and measure the relative importance of each moment involved in the structure model.

D. Summary of the two-way coupling

Since this fluid-structure interaction problem requires the simultaneous solution of the equations of both the structure and the flow, a weakly-coupled partitioned solver is used, as summarized below:

(a)   With the fluid velocity and pressure initialized to the free-stream velocity and zero, respectively, a direct numerical simulation of the unsteady incompressible Navier-Stokes equations is performed, using the feedback forcing formulation of the immersed boundary method, as discussed in Sec. II A.

(b)   The configuration of the reference beams is initialized to the equilibrium angle about which they oscillate while their velocities are initialized to zero. Control volumes around each reference beam and their velocities are defined based on these, and are interpolated to the reference frame of the grid in the fluid domain. The normal and tangential components of the fluid-structure forcing are calculated, based on the fluid velocities in step (a) and velocities at each grid point in the control volumes (cf. Sec. II C 1). The total force at each grid point with index (i, j), denoted by $F_{i,j}^c$, is now transferred to the frame of each reference beam (indexed by k) and denoted there by F_k^c, by integrating it over the corresponding control volumes and multiplying by a smooth hyperbolic scalar field M^c (which has the value 1 on the coating and is zero elsewhere).

(c)   The dynamics of each reference beam is solved (cf. Sec. II C 3).

(d)   With the positions and velocities of each reference beam found in step (c), the positions and velocities at each grid point of the corresponding control volume are interpolated. With these values and the fluid velocities in step (a), the normal and tangential components of the structure-fluid forcing are found. The total force is evaluated by their resultant multiplied by M^c (cf. Sec. II A).

E. Numerical resolution of the structure model

The non-dimensional governing equation (2.7) is solved for each reference beam by using an explicit four-step Runge-Kutta method. Since the mass of the beams considered till now is not too small, use of an explicit method (as opposed to an implicit method) does not cause numerical oscillations, that consequently delay the achievement of the final equilibrium. Between two iterations in the whole fluid-structure interaction model, the dynamics of the coating is calculated explicitly at each temporal sub-iteration.

The aerodynamic performance is measured again in terms of instantaneous as well as time-averaged drag and lift forces, which now also incorporate the force due to the structure on the fluid.

III. RESULTS

A. Aerofoil without control

In order to examine the effectiveness of the poro-elastic coating, the angle of attack at which the lift-to-drag ratio starts to decrease drastically for a smooth aerofoil at incidence, should be determined. For this, computations for angles of attack ranging from $20°$ to $70°$ are carried out. The time-averaged lift coefficients for various angles of attack showed good comparison with the results of Soueid et al.[21] In addition, the results compared well with results from the commercial computational fluid dynamics software FLUENT not only in the time domain but also in the frequency domain.

It is observed that, unlike characteristic stall angles observed in several experiments at high Reynolds numbers, the lift coefficient steadily decreases after around $40°$–$45°$ angle of attack. Besides, the drag continues to increase along with increased fluctuations around this point (cf. Figure 6).

To determine the effectiveness of the feathers in optimizing the lift-to-drag ratio over the entire range of angles, we will consider the physics at the angles of $22°$, $45°$, and $70°$. For this, the signals of the drag and lift coefficients, plotted against time (non-dimensionalized by the free-stream speed and the chord length), are first examined (cf. Figure 7). It is to be noted that the simulations
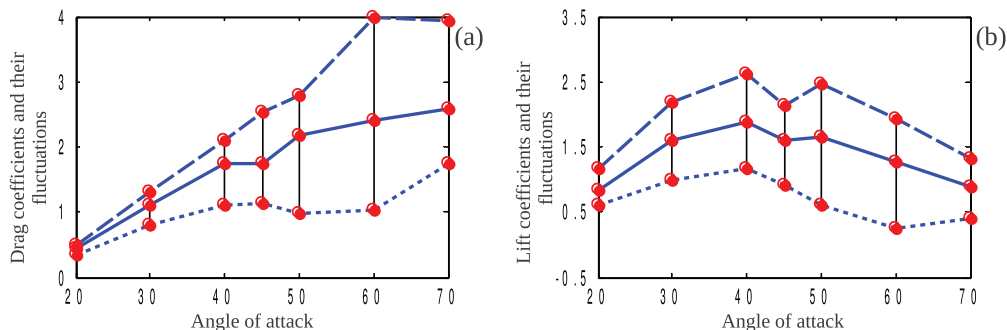

FIG. 6. Dependence of the dimensionless coefficients of (a) time-averaged drag and (b) time-averaged lift, as the angle of attack of a static NACA0012 aerofoil is varied from $20°$ to $70°$. The thick curves represent the mean values of drag and lift, while the dotted curves above and below these thick curves represent the maximum and minimum values of the instantaneous drag and lift coefficients in the course of the oscillations, respectively.
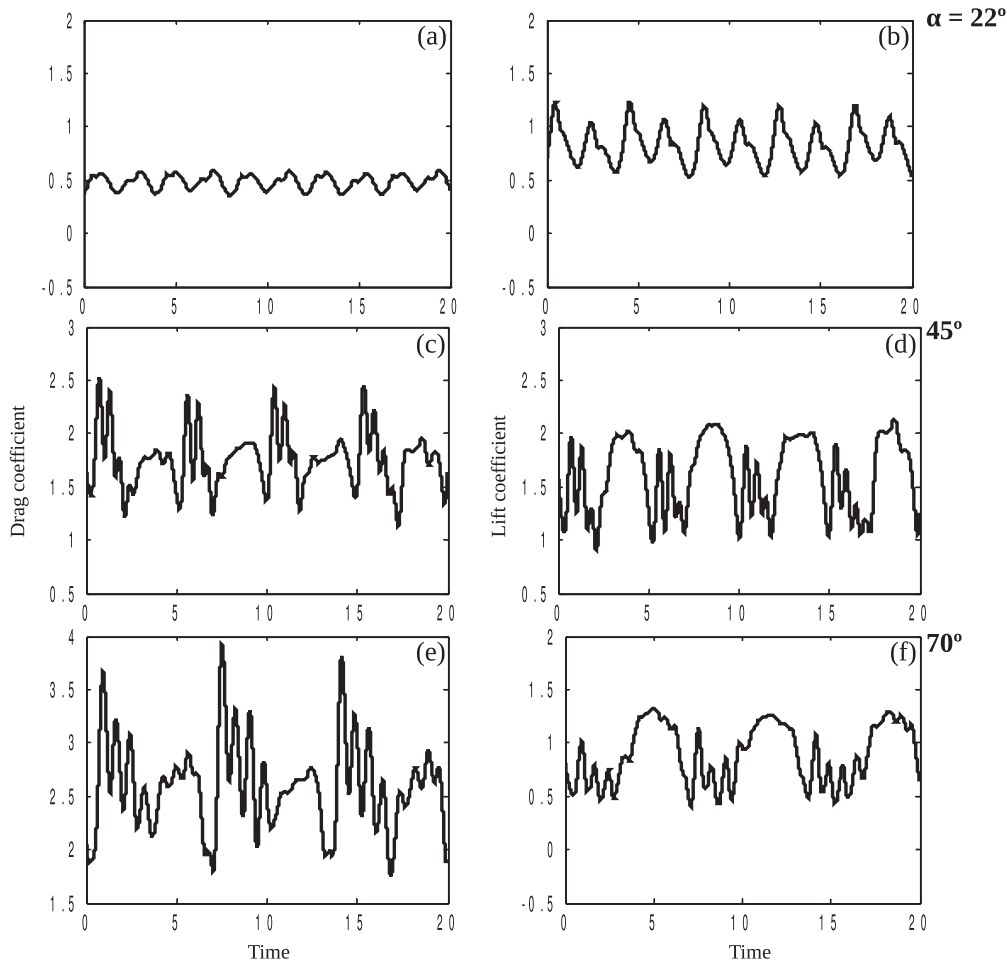
FIG. 7. Time evolution of the drag (left) and lift (right) coefficients for angles of incidence equal to 22° (top), 45° (middle), and 70° (bottom).

conducted in this study are characterized by rather large angles of attack, in order to consider cases of perching manoeuvre (and also owing to the fact that due to a low-Re regime, the angle at which the lift starts to decrease is fairly large at around 45°). Further, the use of long simulation times for such cases can be used to assess the *initial* aerofoil performance during a perching manoeuvre of a bird.

To analyse the release of energy stored in the poro-elastic coating into the boundary layer, which is believed to depend on a frequency synchronisation effect, a Fourier analysis is done for each of these signals. Typically for a small angle of attack, such as 22°, a characteristic frequency is observed in the power spectrum. On the contrary, for higher angles of attack, such as 45° and 70°, this is not so. Further, for these angles, although the frequencies having non-zero contribution in the power spectra of both the drag and lift signals are the same, the amplitudes corresponding to them in these two signals are different (cf. Figure 8). Some physical insight into these observations will be provided in Sec. IV.

B. Investigation of the control parameters

The parameter space: We first summarize the parameters involved in this model. There are three coefficients describing the intrinsic properties of the coating material, namely the rigidity coefficient
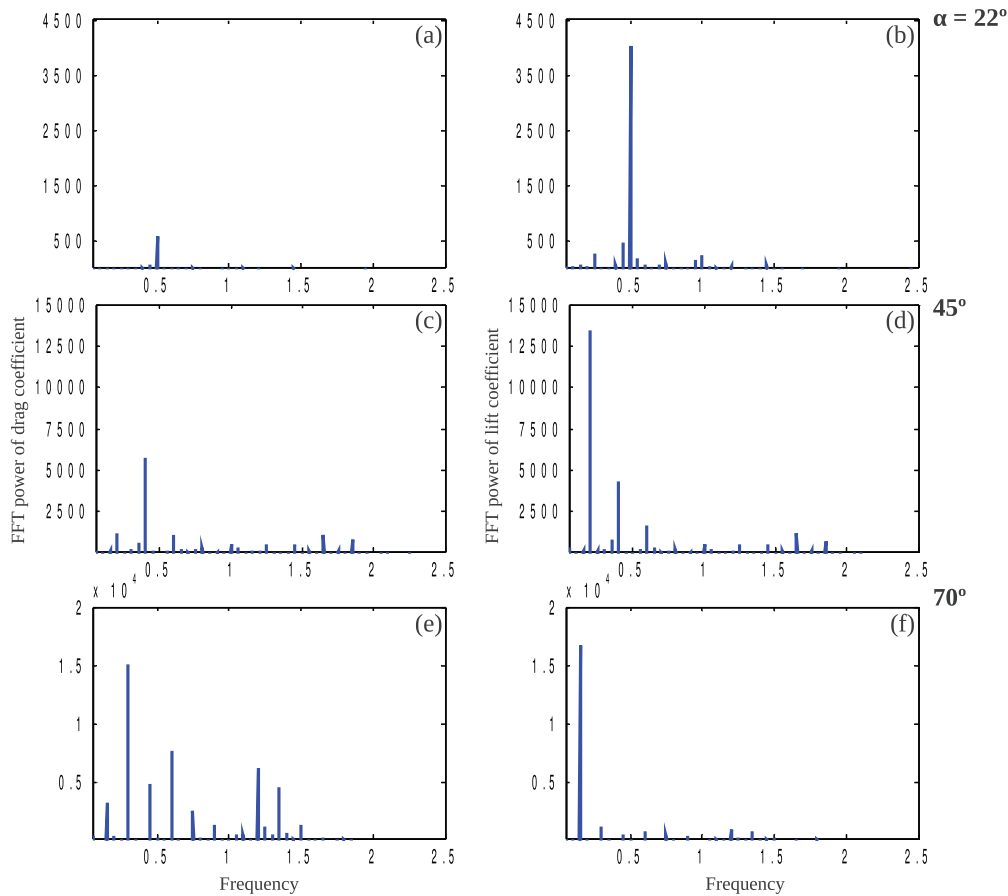
FIG. 8. Power spectra of the drag (left) and lift (right) signals for angles of attack equal to 22° (top), 45° (middle), and 70° (bottom), corresponding to the time signals shown in Figure 7. Non-dimensional frequency is plotted along the horizontal axes.

K_r, the interaction coefficient K_i and the dissipation coefficient K_d, as outlined in Sec II C 2. We also have the parameters corresponding to the equilibrium angle θ_{eq}, the minimum and the maximum angles θ_{min} and θ_{max}, by which each reference element can deflect. Then, there are the parameters giving the physical dimensions of each reference beam, which is a thin circular cylinder – namely the mass m, the length l, and its diameter d_c. Finally, we have the parameters that describe the concentration as well as the relative placement of the coating on the aerofoil, namely the packing density ϕ, the number of reference beams N used to approximate the whole layer; and the coordinates of the points on the aerofoil between which the coating is defined.

Choice of a suitable parameter subset: As indicated in Sec. II C 3, rigidity effects are taken to predominate the structure model. This assumption helps in choosing a few crucial parameters out of the large parameter space outlined in the previous paragraph. The parameters which are fixed for the whole investigation include N, l, d_c, and m. Also, the location of the coating is fixed to 70% of the suction side of the aerofoil, a little away from the leading edge (cf. Table II). The aerofoil is kept smooth close to the trailing edge, because in the case of 22°, the trailing edge vortices were observed to orient the feathers close to the trailing edge almost orthogonally to the flow, which led to some drop in aerodynamic performance. The fixing of the location and extent of the coating, along with fixed N, sets the distance h between two adjacent reference beams, which figures in the definition of the interaction moment. Next, for this fixed h, l is taken equal to 8.5% of the aerofoil chord length, to effectively model non-bending feathers. Further, l, apart from appearing in the definition of the

moment due to the force from the fluid, also figures in the moments due to interaction and inertia (which are taken to be less significant than other terms). The bristles' diameter d_c appears in the definition of the normal and tangential components of the force between the fluid and the structure. As mentioned by Favier et al.,[17] this model is in accordance to those developed by Koch and Ladd[22] and Howells,[23] which are valid only for moderate normal and tangential Reynolds numbers Re_n^h and Re_t^h (defined in Sec. II C 1). Here d_c is fixed such that both Re_n^h and Re_t^h do not exceed the value of 10. Finally m, which figures only in the small contribution from the moment due to inertia, is fixed to a suitable value equal to 12 (non-dimensionalized with respect to the mass of the fluid trapped within a control volume surrounding a reference feather).

The parameters which were extensively studied are K_r and ϕ. K_r was tuned according to the dominant frequencies observed in the uncontrolled flow, which correspond to the frequencies of vortex shedding, as seen from the power spectra of the drag and lift signals for the smooth aerofoil. For each of the values of K_r, K_d was set so that γ (as defined in Sec. II C 3) is equal to 0.05, according to the linear stability analysis by Favier et al.[17] Next, K_i was fixed to satisfy the identity $\omega_d < \omega_i < \omega_r$, where ω_r, ω_i, and ω_d have been defined before in Sec. II C 3. Further, to have favourable comparison of $\dfrac{\mathcal{F}_n^c}{\mu U_n^c}$ and $\dfrac{\mathcal{F}_t^c}{\mu U_t^c}$ to the theoretical model of Howells,[22] ϕ was chosen to lie roughly in the range [0.001, 0.01]. With the parameters chosen as above, now the values for θ_{eq}, θ_{min}, and θ_{max} need to be tuned. As for the parameter θ_{eq}, in the case of the angle of attack of 22°, $\theta_{eq} = 0$ (i.e., the initial orientation of the reference beams being parallel to the free-stream) was seen to yield better aerodynamic performance. Hence, for the other angles of attack of 45° and 70°, this configuration was fixed. Finally, for each of these angles of attack, the angular sector [θ_{min}, θ_{max}] was chosen to have as high compliance as possible, although always restricting the dynamics of the beams to acute positive angles.

C. Aerofoil with control

To control flow separation, it is necessary to optimize the release of energy stored in the boundary layer, at appropriate instants of time. Thus, the idea behind finding the right physical and structural parameters for the poro-elastic coating is to synchronize the vortex shedding and the structures' time scales, to try and trigger a near-resonant response capable of affecting profoundly the physics of this coupled problem. In the light of the fact that the rigidity forces are taken to be predominant, this problem boils down to finding the rigidity parameter K_r, for which the corresponding structure frequency ω_r has a major contribution in the power spectra of the drag or lift signals. Effective non-dimensional control parameters are provided in Tables I and II. With the parameter K_r so chosen and other parameters fixed as described in the previous paragraph, we get enhanced performance for all the three angles of attack of 22°, 45°, and 70°. Specifically, we get 34.36% and 7.5% mean lift increase for 22° and 70°, respectively; and 8.92% and 4.92% mean drag reduction for 45° and 70° respectively. In addition, we obtain 35.47%, 10.46% and 9.71% reduction in drag

TABLE I. Parameters which have been varied in the course of the parametric search; the values provided here are those which guarantee the best control results. The normalization of the structure moments and the flow frequency is done with respect to the mass of the reference beam M, half the length of the reference beam l_c and the time scale of the free-stream, which is the ratio between the aerofoil chord length D and the free-stream speed u_∞.

Angle of attack, α (degrees)	Rigidity moment, K_r	Interaction moment, K_i	Dissipation moment, K_d	Packing density, ϕ	Angular sector of movement, [θ_{min}, θ_{max}] (degrees)	Flow frequency, ω_{fluid}
22	8.9905	0.2034	0.0909	0.0085	[−60,21]	0.4772
45	6.8002	0.2034	0.079	0.0022	[−60,60]	0.4151
70	8.9905	0.2034	0.0909	0.0085	[−60,60]	0.4772

TABLE II. Parameters fixed throughout the course of the study. Here, length and diameter of a reference beam are non-dimensionalized with respect to the aerofoil chord length D.

Mass of reference beam, M	12
Length of reference beam, l	8.5×10^{-2}
Diameter of reference beam, d_c	2×10^{-3}
Equilibrium angle/ Initial orientation of reference beams, θ_{eq} (degrees)	0
Extent of the coating	70% of suction side, starting 0.1 units of length after the leading edge and ending 0.2 units before the trailing edge.
Number of reference beams used, N	8

fluctuations for 22°, 45°, and 70°, respectively; and 7.15% reduction in lift fluctuations for 22° (cf. Fig. 9).

Some physical insight into why we get these improvements due to changes in the local flow field, is provided in Sec. IV.
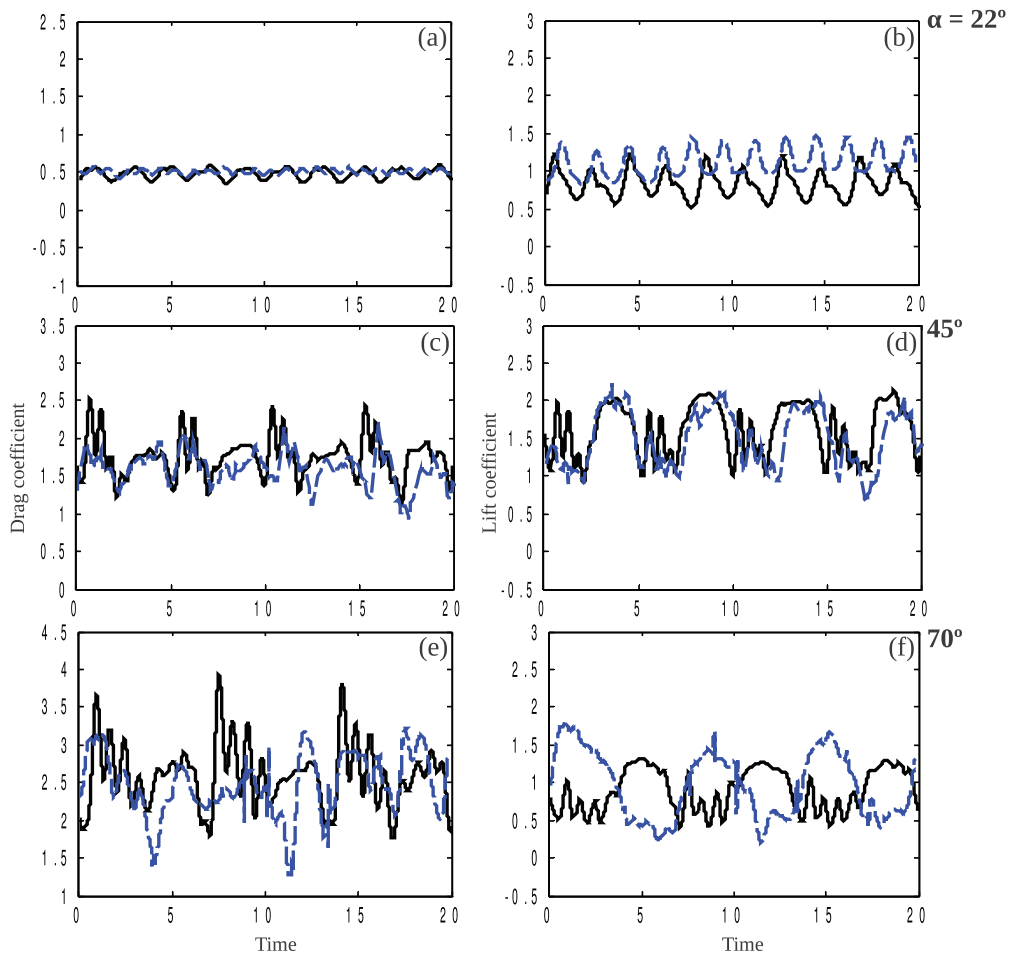

FIG. 9. Time evolution of the drag (left) and lift (right) coefficients for an aerofoil at angles of attack 22° (top), 45° (middle), and 70° (bottom) – comparison between the cases of aerofoil without control (solid, black lines) and aerofoil with control (dashed lines - blue online).
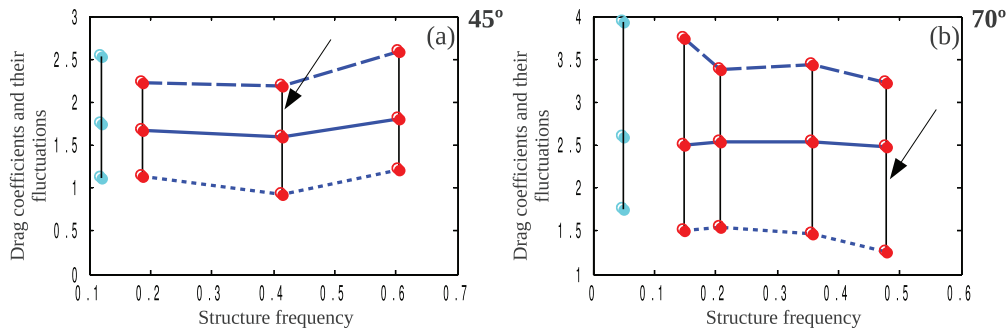
FIG. 10. Dependence of drag on structure frequency (determined by the rigidity moment K_r) for (a) 45° and (b) 70°. The structure frequencies are selected to match frequencies observed in the flow. The thick curves represent the mean values of drag, while the dotted curves above and below these thick curves represent the maximum and minimum values of the instantaneous drag coefficients in the course of the oscillations. The arrows point to the optimum cases shown in Figure 9. In each of these cases, the values of minimum, mean and maximum drag for the reference case (i.e., under uncontrolled conditions) is shown by the black vertical line with light gray dots (cyan online) on the extreme left.

IV. PHYSICAL INTERPRETATION OF THE CONTROL

A. Parametric study

A parametric analysis is done of the change in aerodynamic performance, first by varying the rigidity moment K_r while keeping the packing density ϕ fixed and then by varying ϕ while K_r is fixed at an optimum value. All the other parameters are chosen in accordance with Sec. III B. Although these plots never show regular trends for any of the angles of attack considered, it has been observed that the performance was enhanced (as outlined in Sec. III C) when K_r was such that the dimensionless rigidity frequency was close to 0.4, over other values of K_r. For instance,

(i)   when the angle of attack is 22°, since there was only one frequency, equal to 0.4772, observed in the power spectra of drag and lift signals (cf. Figures 8(a) and 8(b)), only control elements with this rigidity frequency were tested, over an extensive range of packing density (cf. Figure 11(a));

(ii)   in the case of incidence equal to 45°, control elements with rigidity frequency equal to 0.4151 (with a suitable packing density) were seen to produce larger drag reduction, while the mean lift remained roughly unchanged (cf. Figures 10(a) and 11(b));

(iii)   for an angle of 70°, control elements with rigidity frequency equal to 0.4772 (and a suitable packing density) produced higher drag reduction as well as lift enhancement (cf. Figures 10(b) and 11(c)).

So the range of flow frequencies between 0.4 and 0.5 are probably significant to the flow (vis-a-vis the Reynolds number 1100), more than its dependence on the angle of attack. This possibly indicates that for controlling the flow at this Reynolds number, the natural structural frequency should always lie in this range of values.

From the extensive parametric study, as summarized in Figures 10 and 11, it can be seen that it is very important to choose the right control parameters and some other choice is likely to yield sub-optimal results, and possibly even increase in drag and/or decrease in lift accompanied with unfavourable oscillations.

B. Frequencies observed in the fluid-structure coupled system

To see the effects of the control on the flow field, it is important to first analyse the frequencies in the flow for an aerodynamic body with control vis-a-vis the same aerodynamic body without any control. To do this, again a Fourier analysis is done of the controlled signals shown in Figure 9 (depicted by dashed lines-blue online).
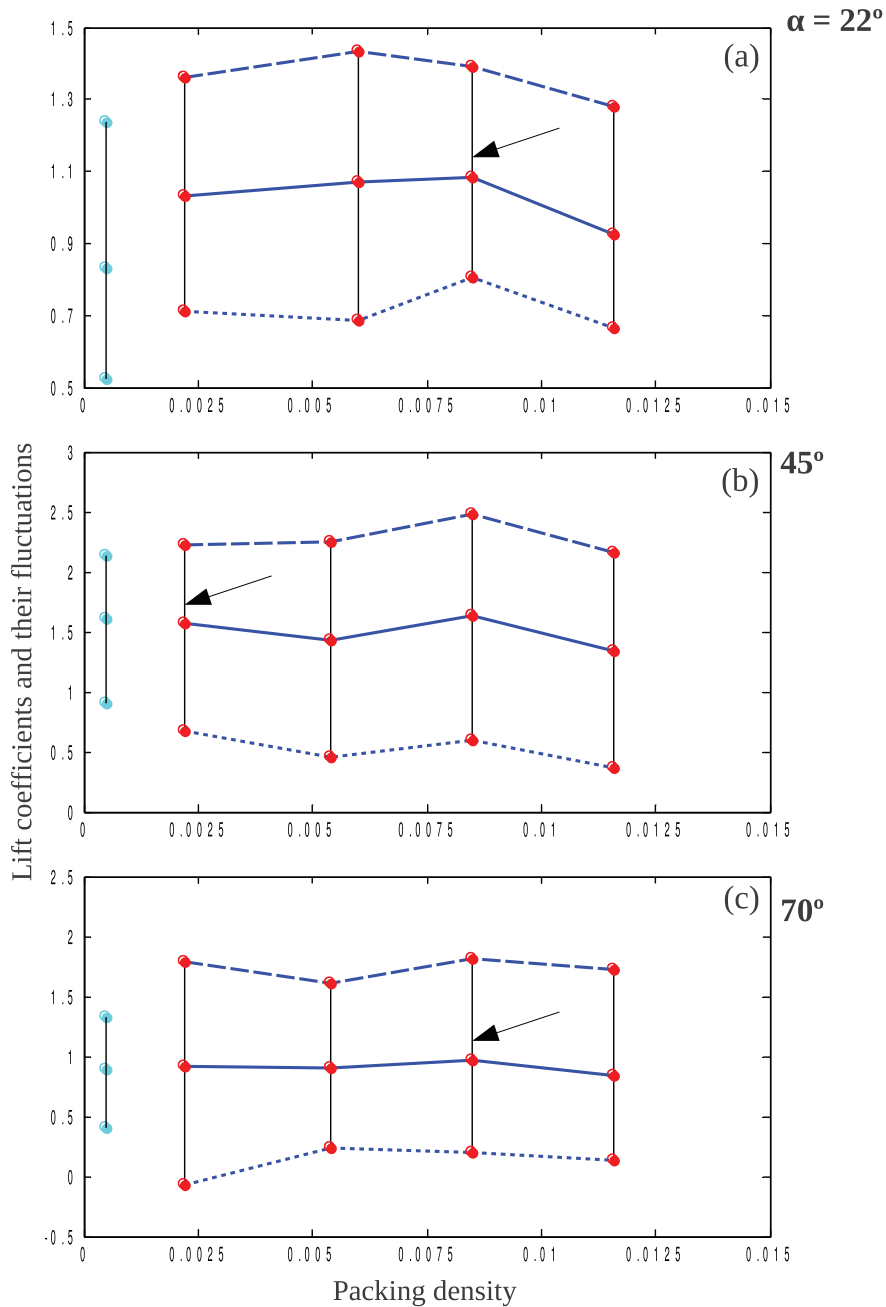
FIG. 11. Dependence of lift as the packing density ϕ is varied over an admissible range (in accordance with Ref. 22) for (a) 22°, (b) 45°, and (c) 70°. The thick curves represent the mean values of lift, while the dotted curves above and below these thick curves represent the maximum and minimum values of the instantaneous lift coefficients in the course of the oscillations. The arrows point to the cases are shown in Figure 9. In each of these cases, the values of minimum, mean and maximum lift for the reference case (i.e., under uncontrolled conditions) is shown by the black vertical line with light gray dots (cyan online) on the extreme left.

The following observations are made for each of the cases:

In the case of an angle of attack of 22°:

(i)   the dominant frequencies in the drag and lift spectra under controlled conditions are generally larger than for a smooth aerofoil;
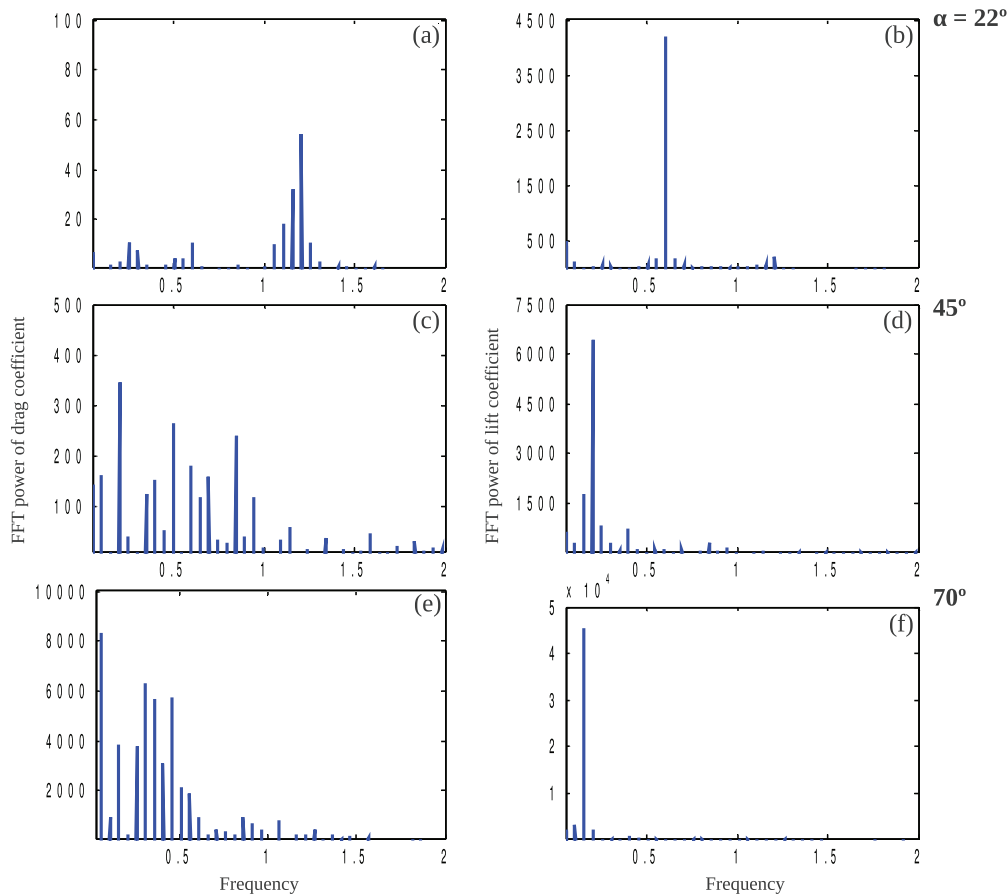
FIG. 12. Power spectra of the drag (left) and lift (right) signals for incidence angles equal to 22° (top), 45° (middle), and 70° (bottom) when the poro-elastic, compliant coating is used, corresponding to the time signals shown in Figure 9 (dashed lines-blue online). Non-dimensional frequency is plotted along the horizontal axes.

(ii)   in the spectrum of the drag signal (cf. Figure 12(a)), there are clusters of frequencies – comprising several frequency components close to each other and in the vicinity of a frequency with maximum amplitude. The dominant frequency (which is close to 1.2 here) is within the last such cluster. However in the lift power spectrum, such frequency clusters are absent and further, only one frequency is observed (cf. Figure 12(b)).

In the cases of angles 45° and 70°:

(i)   the spectra of controlled drag signals show energy spread over a large frequency range (cf. Figures 12(c) and 12(e)), as opposed to what was seen in the uncontrolled cases (cf. Figures 8(c) and 8(e)). In the case of 45°, the range of frequencies measured is centered around the value of 0.4, which was observed to dominate in the spectrum of the uncontrolled drag signal. In the case of 70°, frequencies with values 0.303 and 0.454 are observed, each of which are close to frequencies seen in the spectrum of the uncontrolled drag signal (i.e., 0.3 and 0.45, respectively);

(ii)   the spectra of controlled lift signals (cf. Figures 12(d) and 12(f)) show one dominant frequency in each of these cases – i.e., 0.198 and 0.1515, respectively (both being close to 0.2 and 0.1477 seen in the respective spectra of lift signals in uncontrolled conditions).

Thus, these observations appear to point to a frequency lock-in, or synchronization mechanism, as outlined in Ref. 8.
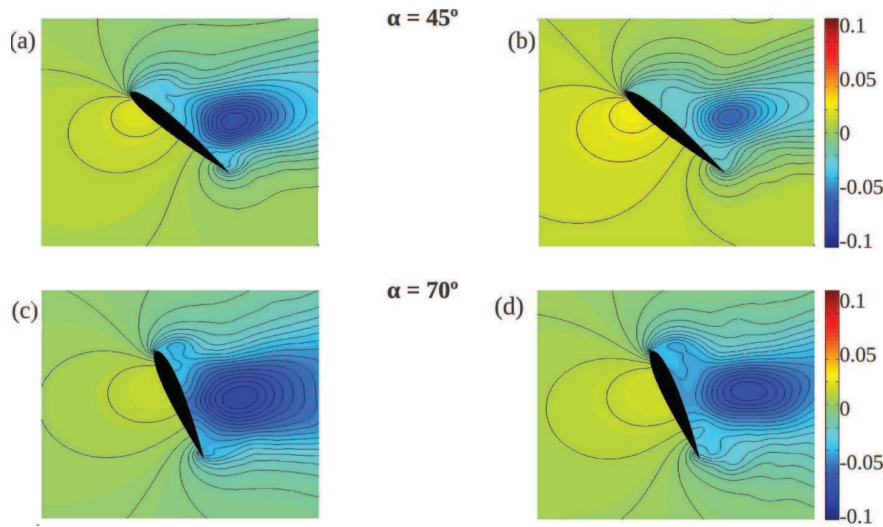
FIG. 13. Time-averaged pressure field, depicted by isolines and shade plot for angles of attack equal to 45° (top) and 70° (bottom). The panel on the left-hand side shows the pressure field for a smooth aerofoil while that on the right-hand side is for a coated aerofoil.

C. Changes in flow field close to the aerofoil

Going beyond analysing new frequencies in the flow, we try to associate some physical implications to these by examining the flow fields (taken here to be in terms of the pressure, vorticity, and wake profile) over suitable time windows, when the controlled flow, in each of the cases, has reached a statistically steady state. These time windows are precisely the ones over which the evolution of the instantaneous drag and lift coefficients are shown in Figure 9.

(i)   From the time-averaged pressure plots (cf. Figure 13), we get information on the effect of the coating on the mean pressure field.

In the case of an incidence equal to 45°, there is a smaller mean pressure gradient as well as a smaller magnitude of overall mean pressure on the suction side, which contributes to reduced mean pressure drag and its fluctuations (cf. Figures 13(a) and 13(b)). This is also observed in the case of 70°, however to a lesser extent (cf. Figures 13(c) and 13(d)). In both these cases, it can also be seen that the poro-elastic layer pushes the vortex (shown by the dark gray (dark blue online) "core") farther away from the suction side, hence showing a modification in the vortex shedding process.

(ii)   Once the vortex shedding process reaches a steady state, the vorticity field at any given instant also tells about the noteworthy contribution of the control elements.

Particularly for an angle of 22° there is an increase in the intensity of the shed vortices as well as an appreciable increase in the Strouhal number (cf. Figures 14(a) and 14(b)). Some increase in the vortex intensity can also be seen for an incidence of 70° (cf. Figures 14(c) and 14(d)). This can be related to a change in the circulation around the aerofoil which in turn explains an appreciable variation in lift in both cases. Further, in the case of 22°, one also sees a noticeable regularization in the vortex shedding phenomenon and a shortening of the length scales of the vortices. In all cases it appears that the time-mean wake is narrower in the vertical direction whenever the bristles are present on the upper surface of the aerofoil, and this has a clear consequence on the integral momentum budget and, more particularly, on the drag force experienced by the aerofoil.
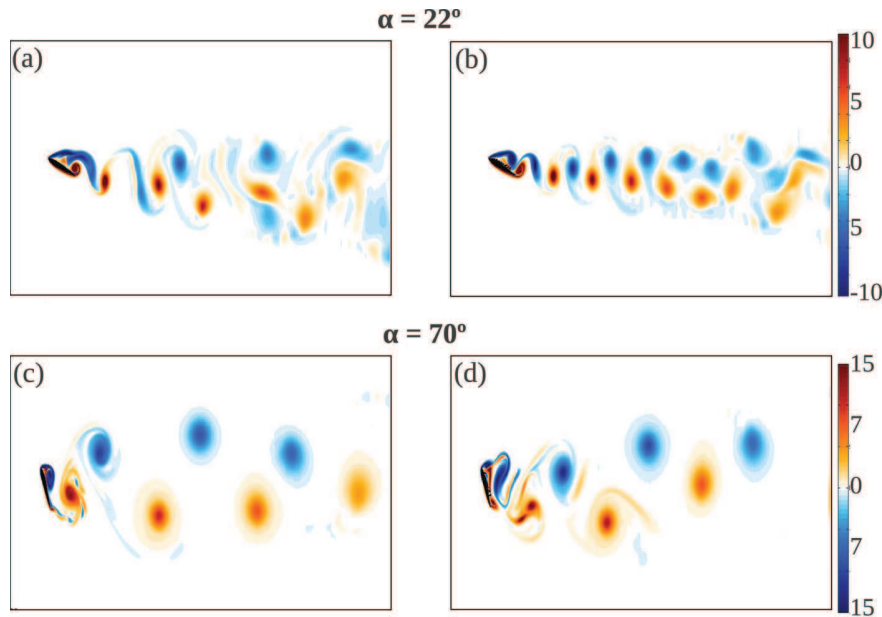
FIG. 14. Shade plot (colour online) of instantaneous vorticity field for angles of attack equal to 22° (top) and 70° (bottom). Left-hand side and right-hand side panels depict uncontrolled and controlled cases, respectively. It is interesting to note that, in the presence of the coating, the shed vortices are more closely spaced than in the corresponding uncontrolled cases.

V. CONCLUSIONS AND PERSPECTIVES

We have numerically studied the passive control of flow separation on a symmetric aerofoil using a dense poro-elastic coating, as a two-way coupled fluid-structure interaction problem. This problem has been dealt with by the immersed boundary technique, wherein the feedback forcing formulation has been used to treat the fluid part (in a Eulerian framework). On the other hand, the force between the fluid and the structure parts (the latter simplified by a discrete set of elements) has been evaluated as the drag force due to flow past a cluster of randomly-oriented, long, thin cylinders. Finally, the discrete set of reference elements for the structure has been modelled as nonlinear spring-mass systems (in a Lagrangian framework). A weakly coupled partitioned solver puts together all these different components of the problem. This study has been an extension of the model for a circular cylinder (developed by Favier et al.[17]), to a complex configuration of a NACA0012 aerofoil.

It is found by a numerical parametric analysis that such a coating – owing to its properties of being porous, compliant, and anisotropic – is able to affect the topology of the flow in the proximity of the rear of the aerofoil, by adapting spontaneously to the separated flow. The coating modifies the vortex shedding process and also positively influences the pressure distribution, hence changing the drag and lift forces as well as their fluctuations. This is achieved by a synchronization of the oscillations of the structures onto a frequency which is comparable to the natural frequency of the fluid system.

For a very low Reynolds number flow, sets of efficient control parameters have been found over 20° to 70° range of angles of attack, where the complete behaviour from the increase to the subsequent drop of the lift coefficient with the incidence angle is observed. This wide spectrum of angles of attack is effectively captured by three angles – 22° (representing the "before-stall" regime), 45° (representing the "near-stall" regime), and 70° (representing the "after-stall" regime). For instance, these passive actuators, with the right kind of properties, are capable of producing a high lift enhancement of more than 30% (for 22°) and a moderate lift increase of around 8% (for 70°); a noteworthy drag reduction of around 9% (for 45°) and a moderate drag reduction of around 5% (for 70°). In addition the drag and lift fluctuations also see positive impact.

Future research, to study the robustness of this passive control method, can possibly include study on more complex configurations such as asymmetric and/or pitching aerofoils. Another extension can be to study the effectiveness of these actuators under turbulent conditions, in the context of controlling transition to turbulence – an area which has significant implications in the design of conventional aircrafts. In such regimes, where the Reynolds number is much higher, it will be meaningful to add a third spatial component to the existing two-dimensional model. Further, moving in a direction towards more realistically modelling this coating, one possibility would be to explore longer, "bending" feathers (for instance, as outlined in Ref. 24).

Finally, we envision to employ a continuum field theory (for instance, that developed by Gopinath and Mahadevan[25] or Oshino *et al.*[26]) based on the equations of poro-elasticity to model realistic layers in three dimensions, and characterize rigorously, through an optimal control approach, the material properties of various types of coatings which are found to be efficient in managing the fluid flow.

ACKNOWLEDGMENTS

[1] M. Gad-el-Hak, *Flow Control: Passive, Active, and Reactive Flow Management* (Cambridge University Press, London, U.K., 2000).

[2] D. J. Pines and F. Bohorquez, "Challenges facing future micro-air-vehicle development," J. Aircr. **43**(2), 290 (2006).

[3] D. W. Bechert, M. Bruse, W. Hage, and R. Meyer, "Biological surfaces and their technological application – laboratory and flight experiments on drag reduction and separation control," AIAA paper No. 97–1960, 1997.

[4] J. B. Anders, "Biomimetic flow control," AIAA paper No. 2000–2543, 2000.

[5] Y. Lian and W. Shyy, "Laminar-turbulent transition of a low Reynolds number: Rigid or flexible airfoil," AIAA J. **45**(7), 1501 (2007).

[6] J. H. M. Fransson, A. Talamelli, L. Brandt, and C. Cossu, "Delaying transition to turbulence by a passive mechanism," Phys. Rev. Lett. **96**, 064501 (2006).

[7] O. Doaré, B. Moulia, and E. de Langre, "Effect of plant interaction on wind-induced crop motion," ASME J. Biomech. Eng. **126**, 146 (2004).

[8] C. Py, E. de Langre, and B. Moulia, "A frequency lock-in mechanism in the interaction between wind and crop canopies," J. Fluid Mech. **568**, 425 (2006).

[9] R. D. Mehta, "Aerodynamics of sports balls," Annu. Rev. Fluid Mech. **17**, 151 (1985).

[10] R. Bannasch, E. Maier, J. Schoffer, M. Stache, and I. Rechenberg, "Drag reduction by slotted wing tips in soaring birds," J. Ornithology **135**(1), 38 (1994).

[11] C. Brücker, J. Spatz, and W. Schröder, "Feasibility study of wall shear stress imaging using microstructured surfaces with flexible micropillars," Exp. Fluids **39**(2), 464 (2005).

[12] J. U. Schlüter, "Lift enhancement at low Reynolds numbers using self-activated movable flaps," J. Aircr. **47**(1), 348 (2009).

[13] N. M. Bakhtian, H. Babinsky, A. L. R. Thomas, and G. K. Taylor, "The low Reynolds number aerodynamics of leading edge flaps," in *Proceedings of the 45th AIAA Aerospace Sciences Meeting and Exhibit, January 8-11, 2007, Reno, NV* (AIAA, Reston, VA, 2007), pp. 8018–8030.

[14] R. Meyer, W. Hage, D. W. Bechert, M. Schatz, T. Knacke, and F. Thiele, "Separation control by self-activated movable flaps," AIAA J. **45**(1), 191 (2007).

[15] C. Brücker, "Interaction of flexible surface hairs with near-wall turbulence," J. Phys.: Condens. Matter **23**, 184120 (2011).

[16] D. Venkataraman and A. Bottaro, "Flow separation control on a NACA0012 airfoil via a porous, compliant coating," in *IFMBE Proceedings of the 6th World Congress on Biomechanics, August 1–6, 2010, Singapore*, edited by C. T. Lim and J. C. H. Goh (Springer, 2010), Vol. 31(1), pp. 52–55.

[17] J. Favier, A. Dauptain, D. Basso, and A. Bottaro, "Passive separation control using a self-adaptive hairy coating," J. Fluid Mech. **627**, 451 (2009).

[18] C. H. Bruneau and I. Mortazavi, "Numerical modelling and passive flow control using porous media," Comput. Fluids **37**(5), 488 (2008).

[19] C. S. Peskin, "The immersed boundary method," Acta Numerica **11**, 479 (2002).

[20] E. A. Fadlun, R. Verzicco, P. Orlandi, and J. Mohd-Yusof, "Combined immersed-boundary finite-difference methods for three-dimensional complex flow simulations," J. Comput. Phys. **161**, 35 (2000).

[21] H. Soueid, L. Guglielmini, C. Airiau, and A. Bottaro, "Optimization of the motion of a flapping airfoil using sensitivity functions," Comput. Fluids **38**(4), 861 (2009).

[22] D. L. Koch and A. J. C. Ladd, "Moderate Reynolds number flows through periodic and random arrays of aligned cylinders," J. Fluid Mech. **349**, 31 (1997).

[23] I. D. Howells, "Drag on fixed beds of fibre in slow flow," J. Fluid Mech. **355**, 163 (1998).

[24] S. B. Lindström and T. Uesaka, "Simulation of the motion of flexible fibers in viscous fluid flow," Phys. Fluids **19**, 113307 (2007).

[25] A. Gopinath and L. Mahadevan, "Elastohydrodynamics of wet bristles, carpets and brushes," Proc. R. Soc. A London **467**, 1665 (2011).

[26] C. Oshino, M. Reyssat, E. Reyssat, K. Okumura, and D. Quéré, "Wicking within forests of micropillars," Europhys. Lett. **79–5**, 56005 (2007).